University of Pavia

Faculty of Engineering — Department of Civil Engineering

Master's Degree in Environmental Engineering

Thesis carried out at:

InLab — Inorganic Nanochemistry Laboratory, Department of Chemistry

MASTER THESIS

Macroscopic Silica Monoliths with Embedded Silver Nanoparticles for Safe Point-of-Use Water Disinfection Avoiding Nanopollution

Candidate:

Mohammad Sadegh Tavakkolian Akbari

Supervisor:

Prof. Piersandro Pallavicini

A.Y. 2025/2026

Abstract

Silver nanoparticles (AgNPs) are widely recognized as effective broad-spectrum antimicrobial agents, acting through the sustained oxidative release of Ag^+ ions. Their incorporation into point-of-use (POU) water disinfection devices is an active area of research, yet most existing systems rely on surface-immobilized AgNPs that can detach and contaminate treated water with intact nanoparticles, raising both environmental and regulatory concerns.

In this work, macroscopic silica monoliths (diameter ~1 cm, mass ~103 mg) with physically embedded AgNPs were prepared by a base-catalyzed sol–gel process using tetramethyl orthosilicate (TMOS). AgNPs (~40 nm, PDI 0.176, $\zeta = -31.7$ mV) were synthesized by citrate–tannic acid co-reduction and incorporated at three loadings (1×, 10×, 100×). STEM-EDS and XRPD confirmed nanoparticle embedding. The silica pore diameter (~2–3 nm) physically prevents nanoparticle release while allowing Ag^+ diffusion.

Ag^+ release was quantified by ISE and ICP-OES. At room temperature using 0.1 M $NaNO_3$ as the medium for ISE and bi-distilled water for ICP-OES, the 100× monolith released 0.065 ppm (ICP-OES) at 24 h. Release was strongly pH-dependent (pH 4.0: 0.621 ppm vs. pH 7.5: 0.054 ppm by ICP-OES at 24 h) and approximately doubled at 37 °C. ISE–ICP discrepancies were observed, reflecting silver speciation (acetate and chloro complexes).

All three loadings achieved >99% CFU reduction of *Escherichia coli* and ***Staphylococcus aureus*** after 24 h at 37 °C in PBS (100×: ME = 4.07 vs. *E. coli*, ME = 2.65 vs. *S. aureus*). Monoliths in a tea-bag configuration achieved equivalent 24 h performance, demonstrating practical feasibility for on-demand POU disinfection.

Acknowledgements

I would like to express my sincere gratitude to my supervisor, Prof. Piersandro Pallavicini, for his continuous guidance, scientific insight, and generous support throughout this research. I am grateful to all members of the research group at the Department of Chemistry, University of Pavia, for their assistance with laboratory work and characterization, and to the technical staff of the ICP-OES and electron microscopy facilities.

Finally, I thank my family for their unwavering encouragement and patience throughout my studies.

Table of Contents

List of Figures

Figure

De
scription **Page**

List of Tables

List of Symbols and Abbreviations

AgNPs	Silver nanoparticles
AgNP⊂SiO₂	Silica monolith with embedded silver nanoparticles
CFU	Colony-forming units
DLS	Dynamic light scattering
DLVO	Derjaguin–Landau–Verwey–Overbeek (theory)
DMF	N,N-Dimethylformamide (drying control chemical additive)
EDL	Electrical double layer
ICP-OES	Inductively coupled plasma optical emission spectrometry
ISE	Ag^+-selective ion electrode
LSPR	Localized surface plasmon resonance
ME	Microbicidal effect (log_{10} CFU reduction)
$NaNO_3$	Sodium nitrate
PBS	Phosphate-buffered saline
PDI	Polydispersity index
POU	Point-of-use
RCF	Relative centrifugal force
ROS	Reactive oxygen species
STEM-EDS	Scanning transmission electron microscopy–energy-dispersive X-ray spectroscopy
TA	Tannic acid
TMOS	Tetramethyl orthosilicate
TGA	Thermogravimetric analysis
WHO	World Health Organization
XRPD	X-ray powder diffraction
α	Chemical activity
γ	Activity coefficient / surface tension
ζ	Zeta potential (mV)

E	Electrode potential (mV)
E^o	Standard electrode potential (mV)
K_{sp}	Solubility product constant
S	Nernstian slope (mV/decade)
μ	Ionic strength (mol/L)

Chapter 1. Introduction

1.1 Global Challenge of Drinking Water Contamination

Access to safe drinking water remains one of the most pressing public health challenges of the twenty-first century. According to the World Health Organization (WHO), hundreds of thousands of people die each year from diarrheal diseases directly associated with the consumption of microbiologically unsafe water [2]. The WHO Guidelines for Drinking-Water Quality enumerate dozens of waterborne pathogens — including bacteria, viruses, and protozoa — that may be present in inadequately treated water supplies [2]. The burden of these diseases falls disproportionately on rural and peri-urban populations in low-income regions that lack access to centralized water treatment infrastructure.

In this context, point-of-use (POU) water disinfection devices have attracted considerable attention as practical and affordable alternatives to large-scale treatment plants. Such devices must function without electrical power, be mechanically simple and durable, low in cost, and operable without specialized technical knowledge. Among the disinfection strategies available, silver-based antimicrobial materials have emerged as one of the most promising approaches, owing to the broad-spectrum bactericidal activity of silver ions (Ag^+) [3].

1.2 Silver Nanoparticles as Antimicrobial Agents

Silver nanoparticles (AgNPs) exhibit significantly enhanced chemical reactivity compared to bulk silver, owing to their high surface-area-to-volume ratio and facile susceptibility to oxidative dissolution. The primary antimicrobial

mechanism is the sustained oxidative dissolution of metallic silver (Ag^0) in the presence of O_2 and H^+:

$$4\,Ag^0(s) + O_2(aq) + 4\,H^+(aq) \rightleftharpoons 4\,Ag^+(aq) + 2\,H_2O(l) \quad (1.1)$$

Ag^+ ions exert bactericidal effects through multiple synergistic mechanisms: binding to thiol groups (–SH) of bacterial proteins and enzymes, inhibiting DNA replication, and generating reactive oxygen species (ROS) that damage cell membranes [4,5]. This multi-target action makes resistance development considerably less likely than for conventional antibiotics. The synthesis of AgNPs by a citrate–tannic acid co-reduction method produces nanoparticles with controlled size and stability. Tannic acid (TA) acts as the primary reducing agent, donating electrons from its multiple phenolic hydroxyl groups arranged around a central glucose core (Figure 1.1), while sodium citrate serves primarily as a stabilizing capping agent.

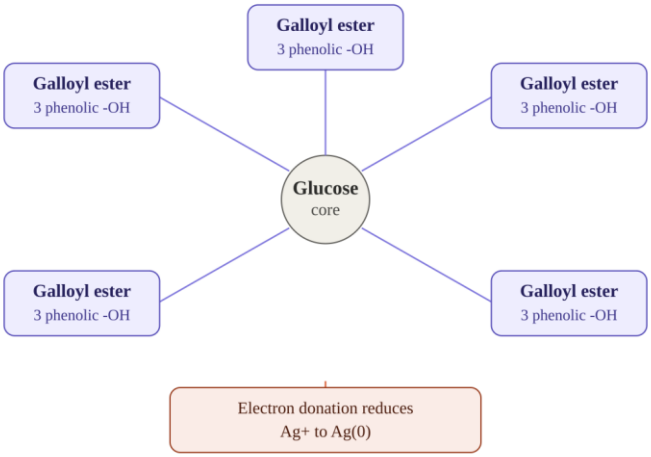

Figure 1.1. Schematic representation of tannic acid, showing the central glucose core esterified with five galloyl ester units, each bearing three phenolic -OH groups responsible for Ag^+ reduction.

1.3 Current Approaches and Their Limitations

A wide variety of support materials have been explored for AgNP-based water disinfection, including cellulose filters [5], woven microfiltration membranes [6], ceramic supports [7,8], ion-exchange resins [9], cotton fabrics [10], and silica-based materials [5-12]. In virtually all these systems, AgNPs are deposited on the support surface. Although effective, this approach carries an inherent limitation: intact AgNPs can detach and enter the treated water (Figure 1.3A), raising regulatory concerns. Commission Regulation (EU) No 10/2011 permits nanoparticles in food-contact materials only when their release is demonstrably prevented [15]. European Union regulations also require that nanoparticle migration into food is impossible [15], providing a clear motivation for the embedded design.

1.4 Silica Monoliths as Host Matrices

Porous silica prepared by the sol–gel process is chemically inert, non-toxic, and structurally versatile material. The primary precursor used in this work, TMOS ($Si(OCH_3)_4$), undergoes base-catalyzed hydrolysis and polycondensation to build a rigid siloxane network (Figure 1.2). When AgNPs are incorporated into the precursor sol prior to gelation, they become physically entrapped. Since TMOS-derived silica exhibits pore diameters of 2–3 nm — well below the ~36 nm AgNP diameter — nanoparticles are permanently retained while Ag^+ ions freely diffuse through the pores (Figure 1.3B)[21].

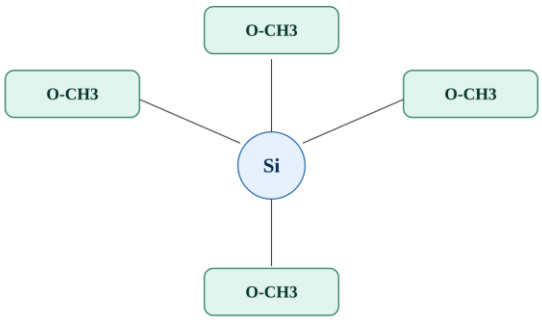

Si(OCH3)4 - hydrolyzes to silanol, then condenses to SiO2

Figure 1.2. Molecular structure of TMOS ($Si(OCH_3)_4$). Hydrolysis of $Si-OCH_3$ bonds yields silanol intermediates that condense to form the SiO_2 matrix.

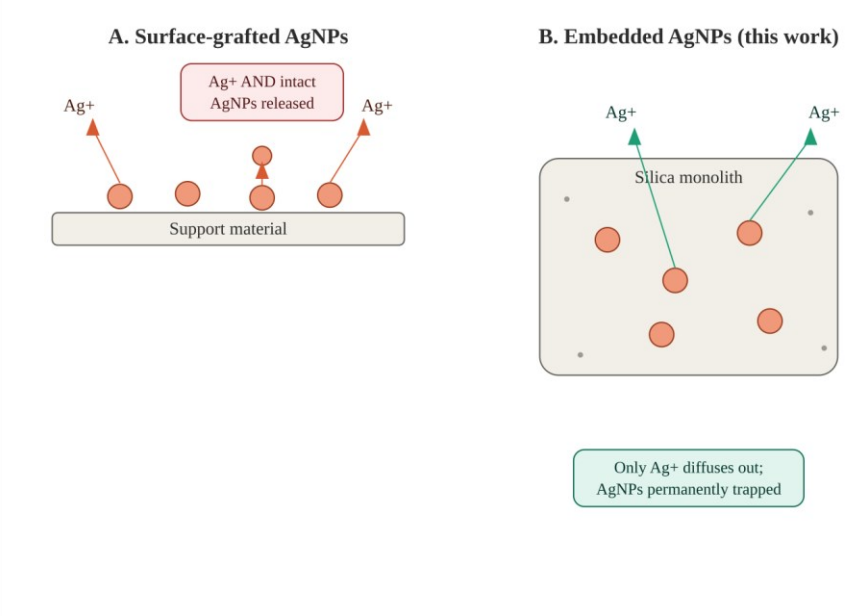

Figure 1.3. (A) Surface-grafted AgNPs: both Ag^+ ions and intact nanoparticles are released into treated water. (B) Embedded AgNPs (this work): nanoparticles are permanently retained within the silica bulk; only Ag^+ ions diffuse out through the nanopores.

1.5 Research Objectives

The present thesis was carried out with the following specific objectives:

1. To synthesize colloidal AgNPs (~40 nm) by citrate–tannic acid co-reduction and characterize their physicochemical properties by UV–Vis absorption spectroscopy, TEM, DLS, and zeta potential.
2. To prepare macroscopic silica monoliths with embedded AgNPs at three loadings (1×, 10×, 100×, corresponding to a total of 10.9, 109, and 1090 Ag micrograms per single monolith, respectively) via TMOS sol–gel, and verify nanoparticle retention by absorption spectroscopy, STEM-EDS and XRPD.

3. To quantify Ag^+ release under varying conditions (loading, pH 4.0–7.5, temperature 20– 37 °C) using ISE and ICP-OES, and rationalize the trends in terms of electrochemical and thermodynamic principles.
4. To evaluate antimicrobial efficacy against *E. coli* and *S. aureus* in planktonic suspension and correlate ME with Ag^+ release data.
5. To demonstrate a practical tea-bag application mode for on-demand POU water disinfection.

Chapter 2. Literature Review

2.1 Global Water Crisis and Waterborne Disease Burden

The World Health Organization (WHO) estimates that unsafe water, inadequate sanitation, and poor hygiene collectively cause over 1.4 million deaths annually, with the majority attributable to diarrheal diseases [2]. Waterborne pathogens — bacteria (*Vibrio cholerae*, *Salmonella typhi, pathogenic E. coli*), viruses (rotavirus, norovirus, hepatitis A), and protozoa (*Cryptosporidium parvum, Giardia lamblia*) — represent the primary infectious agents transmitted through contaminated drinking water [2]. Approximately 2 billion people globally still consume water from fecally contaminated sources [2].

The consequences are not limited to mortality: chronic low-level exposure to waterborne pathogens causes stunting, malnutrition, and impaired cognitive development in children. For rural communities, disaster-affected populations, and remote areas without grid connectivity, POU technologies represent the most practical and immediately deployable solution. According to WHO performance specifications, POU water treatment technologies should achieve at least a 2-log bacterial reduction, at least a 3-log viral reduction, and at least a 2-log protozoan reduction to be classified as providing a protective level of protection [36]. Silver-based POU technologies are particularly attractive because they offer broad-spectrum antimicrobial activity without electrical power, chemical consumables, or specialized maintenance.

2.2 Silver as an Antimicrobial Agent

2.2.1 Historical Background

The use of silver for antimicrobial purposes predates modern microbiology by millennia. Ancient Greek, Roman, and Phoenician civilizations stored water and wine in silver vessels to prevent spoilage. In the nineteenth century, silver nitrate was adopted clinically for prophylaxis against ophthalmia neonatorum and for burn wound treatment. The emergence of antibiotic-resistant bacteria has renewed scientific interest in silver-based antimicrobials [4].

2.2.2 Mechanisms of Antimicrobial Action

The bactericidal activity of silver is primarily mediated by Ag^+, generated by oxidative dissolution of Ag^0. Ag^+ exerts toxicity through multiple synergistic mechanisms [4,5]:

- Protein and enzyme inhibition: Ag^+ ions bind with high affinity to thiol groups (–SH) of cysteine residues in bacterial proteins and metalloenzymes, disrupting the respiratory chain, DNA replication machinery, and cell wall synthesis.
- DNA damage: Ag^+ intercalates with nucleic acids, causing chromosomal condensation and inhibiting DNA replication and transcription.
- Membrane disruption and ROS generation: Ag^+ catalyzes production of hydroxyl radicals and superoxide that oxidize membrane lipids and proteins, increasing permeability and causing cell lysis.
- Biofilm inhibition: sub-lethal Ag^+ concentrations disrupt quorum sensing and inhibit initial adhesion, preventing establishment of disinfectant-resistant biofilms.

The multi-target toxicity of Ag^+ makes resistance development significantly less likely than for conventional single-target antibiotics [4].

2.2.3 Differential Susceptibility of Gram-Positive and Gram-Negative Bacteria

The two major structural classes of bacteria — Gram-negative and Gram-positive — differ profoundly in their cell envelope architecture, and this difference directly determines their susceptibility to silver-mediated killing.

Gram-negative bacteria (e.g., *E. coli, Pseudomonas aeruginosa, Salmonella spp*.) possess a thin peptidoglycan layer (2–3 nm) sandwiched between an inner cytoplasmic membrane and an outer membrane. The outer membrane contains protein channels called porins (OmpA, OmpC, OmpF), which facilitate the passive diffusion of small hydrophilic molecules. Ag^+ ions and neutral silver species can enter through these channels, rapidly reaching the cytoplasm where they exert their toxic effects. The lipopolysaccharide (LPS) component of the outer membrane, while initially repelling positively charged Ag^+, is destabilized at bactericidal silver concentrations, further facilitating entry.

Gram-positive bacteria (e.g., *S. aureus, Bacillus subtilis, Streptococcus spp*.) lack an outer membrane but possess a much thicker, more densely cross-linked peptidoglycan cell wall (20–80 nm). The Gram-positive cell wall is additionally enriched in teichoic acids (TA) and lipoteichoic acids (LTA), polyanionic polymers that carry a net negative charge throughout the cell wall volume. This polyanionic network acts as a powerful electrostatic sink for incoming Ag^+ cations: silver ions become complexed and immobilized within the cell wall matrix before reaching the cytoplasmic membrane. This sequestration mechanism effectively attenuates the intracellular delivery of the active biocide, explaining the systematically lower Microbicidal Effect values observed for *S. aureus* relative to *E. coli* in the present work and in the broader literature [4].

2.3 Silver Nanoparticles: Synthesis and Physicochemical Properties

2.3.1 Advantages of the Nanoscale

Silver nanoparticles (AgNPs) offer several physicochemical advantages over bulk silver and silver salts for antimicrobial applications. First, their

exceptionally high surface-area-to-volume ratio (e.g., a 10 nm AgNP has ~50% of its atoms at the surface) dramatically increases the fraction of silver atoms available for oxidative dissolution and Ag^+ release. Second, the confinement of conduction electrons within nanoscale dimensions gives rise to localized surface plasmon resonance (LSPR), a phenomenon with no analogue in bulk silver, that generates absorption bands at specific wavelengths and facilitate their optical identification and study. Third, AgNPs can be functionalized with diverse capping ligands that control their surface chemistry, stability, and biological interactions. Fourth, the size, shape, and surface charge of AgNPs can be systematically tuned during synthesis to optimize Ag^+ release kinetics for specific applications [18].

2.3.2 Comparison of AgNP Synthesis Methods

A large number of methods have been developed for the synthesis of AgNPs with controlled size and morphology. Table 2.1 provides a systematic comparison of the most widely employed approaches, including the method adopted in the present work.

Method	Reducing agent	Stabilizer	Typical size (nm)	PDI	Key advantages	Key limitations
Turkevich (citrate only)	Sodium citrate (at 95–100°C)	Citrate	20–60	0.15–0.35	Simple; scalable; well-established; food-safe reagents	Slow kinetics; broad PDI; limited size control below 20 nm
Borohydride reduction	$NaBH_4$ (room temp.)	Various ligands	2–10	0.10–0.20	Very small particles; fast; room temperature	$NaBH_4$ is toxic and unstable; particles less stable; not food-safe
Dual-reductant (citrate + TA) [this work]	Tannic acid (primary) + citrate (secondary, at 95–100°C)	Citrate	20–40	0.10–0.20	Narrow PDI; controlled size; green reagents; scalable;	Tannic acid cost; requires optimization of TA:citrate ratio

Method	Reducing agent	Stabilizer	Typical size (nm)	PDI	Key advantages	Key limitations
					excellent colloidal stability	
Polyol process	Ethylene glycol or other polyols (at 120–160°C)	PVP or other polymers	20–200	0.05–0.15	Very narrow PDI; shape control (triangles, cubes)	High temperature; organic solvents; non-aqueous; not green
Green/biological synthesis	Plant extracts, microorganisms, enzymes	Biomolecules (polyphenols, proteins)	10–100	0.20–0.50	Eco-friendly; low cost; renewable reagents	Poor reproducibility; broad PDI; difficult to characterize capping layer; batch variability
Photochemical reduction	UV irradiation or laser ablation	Various	5–50	0.15–0.30	No chemical reductant needed; clean particles	Specialized equipment; slow; difficult to scale up

Table 2.1. Comparison of principal AgNP synthesis methods by reducing agent, stabilizer, typical particle size, polydispersity index (PDI), key advantages, and key limitations.

The dual-reductant approach adopted in the present work — combining tannic acid as the primary reducing agent with sodium citrate as the stabilizing capping agent — was systematically developed by Bastús et al. [17] and Morris et al. [16] as an optimized protocol that overcomes the principal limitations of the (Turkevich) citrate or citrate/$NaBH_4$ methods. The key point is the kinetic decoupling of nucleation (driven by the rapid electron-donation kinetics of tannic acid) from growth (governed by diffusion of remaining Ag^+ precursor to existing nuclei). By generating a large number of nuclei instantaneously, the fixed pool of Ag^+ is distributed among many seeds, limiting growth to yield particles in the 20–40 nm range with PDI < 0.20. The resulting nanoparticles are suitable for sol–gel encapsulation: large enough (>30 nm) to be geometrically

excluded from the 2–3 nm pores of TMOS-derived silica, yet small enough to remain colloidally stable during the gelation process.

2.3.3 Colloidal Stability: DLVO Theory and Zeta Potential

The long-term colloidal stability of AgNP suspensions is governed by the thermodynamic balance between attractive van der Waals forces and electrostatic repulsion between neighboring particles, as formalized in the Derjaguin–Landau–Verwey–Overbeek (DLVO) theory [40]. The total interparticle potential energy is given by:

$$V^{Tot}_{al} = V^{\beta oW} + V^{ILL} \quad (2.1)$$

where $V^{\beta oW}$ represents the attractive van der Waals interactions and V^{ILL} the repulsive Coulombic interactions arising from overlapping electrical double layers (EDL). Electrostatic stabilization is provided by the adsorption of charged capping ligands (citrate anions, $C_6H_5O_7^{3-}$) onto the nanoparticle surface, which generate a negative surface potential (Stern potential) and an extended diffuse double layer that repels neighboring particles.

The zeta potential (ζ), measured at the hydrodynamic shear plane (slipping plane) surrounding the particle, provides a practical experimental proxy for the magnitude of the electrostatic repulsion. A zeta potential more negative than −30 mV is the generally accepted empirical threshold for adequate colloidal stability, indicating that the electrostatic energy barrier is sufficient to prevent spontaneous aggregation under ambient conditions [22]. In the present work, the optimized AgNP batch achieved $\zeta = -31.67 \pm 2.5$ mV, confirming excellent colloidal stability throughout the subsequent sol–gel processing steps.

It is important to note that DLVO stability is highly sensitive to the ionic strength of the medium: increasing ionic strength compresses the EDL (Debye screening), reducing the effective range of the electrostatic repulsion and lowering the energy barrier against aggregation. This has practical implications

for the use of AgNPs in water treatment, where complex ionic matrices (saline water, buffered systems, natural water containing divalent cations such as Ca^{2+} and Mg^{2+}) can trigger aggregation of non-embedded AgNPs. The physical immobilization of AgNPs within the silica matrix in the present work eliminates this stability concern entirely.

2.4 AgNP-Based Water Disinfection: State of the Art

2.4.1 Surface-Decorated Support Materials

Support materials for AgNP-based POU disinfection include cellulose [5], woven membranes [6], ceramic filters [7,8], ion-exchange resins [9], cotton fabrics [10], and silica [11]. Table 2.2 compares the major approaches. In all cases, AgNPs are deposited on the support surface, creating the fundamental risk of nanoparticle detachment under mechanical or hydrodynamic stress [23].

Support material	AgNP attachment method	Particle size (nm)	Tested bacteria	Log reduction	Contact time	Key limitation
Cellulose paper [6]	In situ reduction	4–10	E. coli	> 6	Flow-through	Mechanical fragility; AgNP release in flow
Woven microfiltration membrane [7]	Adsorption + reduction	10–20	E. coli, S. aureus	3–4	10 min	Membrane fouling; AgNP detachment under shear
Ceramic filter [8,9]	Colloidal impregnation	5–20	E. coli, Total coliforms	> 2	Flow-through	Variable pore size; AgNP leaching; cracking
Ion-exchange resin [10]	Ag^+ exchange + reduction	5–15	E. coli	> 4	30 min	Column breakthrough; limited reusability
Cotton fabric + chitosan [11]	Chemical reduction	10–30	E. coli, S. aureus	3–5	60 min	AgNP detachment; fabric degradation
Silica (surface grafted) [12]	Organosilane grafting	10–40	E. coli, S. aureus	2–4	24 h	AgNP and Ag^+ both released; nanopollution risk

Support material	AgNP attachment method	Particle size (nm)	Tested bacteria	Log reduction	Contact time	Key limitation
Silica monolith (embedded) [this work]	Sol–gel entrapment	~ 36	E. coli, S. aureus	2.4–4.1	5–24 h	No nanoparticle release; only Ag^+ diffuses out

Table 2.2. Comparison of AgNP-based water disinfection materials by support type, attachment method, AgNP size, bacterial targets, antimicrobial performance, and key limitations. Data from references [5–11] and this work.

Several important trends emerge from Table 2.2. First, surface-decorated materials generally achieve high log reductions (>3) at short contact times when AgNPs are directly accessible to the bacterial suspension, but all are subject to nanoparticle detachment under mechanical or hydrodynamic stress. Second, the log reduction values reported in the literature are difficult to compare directly, as they depend strongly on the experimental conditions (bacterial concentration, contact time, volume of water, buffer composition, temperature), making standardization of antimicrobial performance claims challenging. Third, no study prior to the present work has systematically combined direct nanoparticle retention verification (by surface imaging and XRPD) with complementary ISE and ICP-OES monitoring of Ag^+ release and a tea-bag application format.

2.4.2 The Nanopollution Problem

The environmental and toxicological implications of AgNP release into drinking water are not yet fully characterized but are a subject of growing regulatory and scientific concern. AgNPs have been detected in effluents from washing machines treating AgNP-containing textiles [23], in treated wastewater from facilities serving hospitals using silver-based wound dressings, and in surface water downstream of industrial discharge points. The ecotoxicological effects of AgNPs include acute and chronic toxicity to aquatic organisms (*Daphnia magna, Danio rerio, Mytilus galloprovincialis*), disruption of soil microbial

communities, and inhibition of wastewater nitrification bacteria at environmentally relevant concentrations [4,30].

For drinking water specifically, the principal concern is the potential for AgNPs to cross the intestinal epithelium upon ingestion, enter systemic circulation, and accumulate in organs (particularly liver, spleen, and kidney). In vitro studies have demonstrated cytotoxic and genotoxic effects of AgNPs on human cell lines (HeLa, Caco-2, THP-1) at concentrations achievable through nanoparticle leaching from disinfection devices used over extended periods. The European Food Safety Authority (EFSA) concluded in 2018 that the available data are insufficient to establish a health-based guidance value for AgNP exposure via food or water, applying the precautionary principle [37].

From a regulatory standpoint, Commission Regulation (EU) No 10/2011 on plastic materials and articles intended to come into contact with food explicitly permits TiO_2, Si_3N_4, and ZnO nanoparticles as functional barriers in food-contact polymers, but only on the condition that nanoparticle migration into food is impossible — i.e., only in the embedded, non-migratory configuration. This regulatory logic directly motivates the embedded AgNP architecture of the present work: by embedding AgNPs within a silica matrix whose nanopore geometry physically prevents nanoparticle migration, while allowing Ag^+ ionic diffusion, the system achieves the optimal combination of antimicrobial efficacy and nanoparticle safety [13].

2.4.3 Embedded AgNP Architectures: Previous Work

To address the nanopollution problem, several research groups have investigated polymer-based matrices for AgNP embedding, including polyurethane foams, poly(vinyl alcohol) hydrogels, and cellulose aerogels. While demonstrating reduced nanoparticle release compared to surface-decorated materials, polymer matrices suffer from several limitations: poor chemical and thermal stability, swelling in aqueous environments that can deform the matrix and expose

embedded particles, and uncertain long-term nanoparticle retention upon mechanical loading.

Silica-based matrices prepared by the sol–gel process represent a fundamentally more robust embedding medium, combining chemical inertness, thermal stability up to ~700 °C, mechanical rigidity, and intrinsically nanoscale porosity [39]. The sol–gel route is particularly well-suited to nanoparticle embedding because the gelation proceeds under mild conditions (room temperature, aqueous or partly aqueous medium, low pH or base catalysis) that are compatible with colloidal nanoparticle suspensions without causing aggregation. Previous work from the Pallavicini group at the University of Pavia demonstrated the feasibility of embedding gold nanoparticles [21] and silver nanoparticles [25] within sol–gel silica matrices, establishing the chemical and process engineering foundation on which the present thesis work builds.

2.5 Sol–Gel Silica: Chemistry, Properties, and Engineering

2.5.1 The Sol–Gel Process: Reaction Mechanism

The sol–gel process is a low-temperature, solution-phase route for the synthesis of amorphous inorganic oxide networks from molecular precursors. For silica, the most commonly employed precursors are tetraalkyl orthosilicates $Si(OR)_4$, of which tetramethyl orthosilicate (TMOS, $Si(OCH_3)_4$) and tetraethyl orthosilicate (TEOS, $Si(OC_2H_5)_4$) are the most widely used. TMOS is preferred over TEOS in the present work because its smaller methoxy groups (relative to ethoxy) are hydrolyzed more rapidly, accelerating gelation and reducing the volume of alcohol byproduct generated.

The overall transformation proceeds through two sequential and partially overlapping reaction classes, each of which can be catalyzed by either acids or bases [39]:

Hydrolysis: The Si–OCH_3 bonds undergo nucleophilic substitution by water molecules, displacing methanol and generating reactive silanol (Si–OH) intermediates. Under base-catalyzed conditions, this proceeds through an SN2-like mechanism in which hydroxide ions attack the electrophilic silicon center:

$$Si(OCH_3)_4 + 4\,H_2O \rightarrow Si(OH)_4 + 4\,CH_3OH \quad (2.2)$$

Condensation: The silanol groups undergo condensation reactions to form siloxane (Si–O–Si) linkages, the covalent bonds that build the three-dimensional network. Two pathways operate simultaneously:

$$\equiv Si–OH + HO–Si\equiv \rightarrow \equiv Si–O–Si\equiv + H_2O \quad (water\ condensation,\ 2.3)$$

$$\equiv Si–OCH_3 + HO–Si\equiv \rightarrow \equiv Si–O–Si\equiv + CH_3OH \quad (alcohol\ condensation,\ 2.4)$$

Under base-catalyzed conditions, the condensation rate constant significantly exceeds the hydrolysis rate constant. This kinetic asymmetry promotes the rapid formation of densely cross-linked, particulate-like clusters that grow and eventually percolate at the gel point, forming a macroscopic three-dimensional network spanning the entire reaction volume. The gel point is the topological threshold at which the growing branched clusters interconnect into a single continuous spanning network: at this point, the system abruptly loses fluidic flow and transitions from a viscous liquid to a viscoelastic solid.

2.5.2 Pore Structure and Size Distribution

The pore structure of the resulting gel is determined by the interplay of reaction kinetics, catalyst concentration, water:silicon molar ratio (r), and drying conditions. Under base-catalyzed conditions with TMOS, the condensation-dominated kinetics promote the formation of dense, compact clusters that pack into a relatively open framework with pore diameters distributed in the 2–5 nm range, as characterized by nitrogen adsorption (BET analysis) in previous studies from the group [21]. This pore size distribution is critical for the success of the

nanoparticle embedding strategy: since the AgNPs synthesized in the present work have a physical core diameter of 36 nm (by TEM), they are geometrically excluded from the silica pores by a factor of ~10–18× in diameter (³~1000× in volume), ensuring permanent physical entrapment.

Water molecules (hydrodynamic diameter ~0.28 nm) and Ag^+ ions (ionic radius 0.115 nm) are, however, one order of magnitude smaller than the pore diameter and diffuse freely through the interconnected pore network. The driving force for Ag^+ diffusion through the monolith is the concentration gradient established between the Ag^+-rich interior (where AgNP oxidative dissolution occurs) and the Ag^+-depleted exterior (the bulk solution). This concentration gradient-driven diffusion follows Fick's first law and gives rise to the sustained, controlled release profile observed experimentally.

2.5.3 Drying Mechanics and Crack Prevention

The conversion of a wet, fluid-filled gel to an intact macroscopic gel without fracture is the principal engineering challenge of the sol–gel process. During solvent evaporation, curved liquid–gas menisci form within the nanopores, generating capillary pressures described by the Young–Laplace equation:

$$\Delta P = 2\gamma \cos\theta / r \quad (2.5)$$

where γ is the surface tension of the pore liquid, θ is the contact angle between the liquid and the pore wall, and r is the pore radius. For pore radii of 1–2 nm and γ = 72 mN/m (water), the resulting capillary pressure can exceed 100 MPa — far beyond the tensile strength of the fragile, incompletely condensed gel network. This generates destructive tensile stresses that cause the monolith to fracture into fine powder during drying if no mitigating strategy is applied.

Several strategies have been developed to mitigate crack formation, and in the present work they are combined synergistically: (i) Aging of the wet gel under Parafilm® seal for 3 days before opening, allowing continued syneresis (slow

condensation of residual silanol groups) to thicken the pore walls and increase their tensile strength; (ii) Controlled, slow opening of the Parafilm® to allow gradual, equilibrium-limited solvent evaporation rather than rapid, stress-generating flash evaporation; (iii) Addition of DMF as a drying control chemical additive (DCCA), which reduces the surface tension of the pore liquid and promotes uniform pore emptying by establishing a more homogeneous evaporation front across the monolith cross-section; (iv) Moderate thermal drying at 70 °C, which is below the boiling point of DMF (153 °C) and avoids violent gas generation within the pores. The combination of these measures yields crack-free or minimally fractured monoliths in approximately 25% of the wells, with the remaining wells producing 2–6 fragments that are functionally equivalent for all antimicrobial and release experiments.

2.6 Regulatory Framework for Silver in Drinking Water

The regulatory landscape governing the use of silver in drinking water and food-contact applications is complex, evolving, and varies significantly across jurisdictions. The key regulatory instruments relevant to the present work are summarized below.

The World Health Organization (WHO) sets a guideline value of 0.1 mg/L (0.1 ppm) for silver in drinking water, established on the basis of aesthetic considerations (prevention of argyria, a permanent bluish-gray skin discoloration caused by chronic Ag^+ overexposure) rather than acute toxicological endpoints [15]. This guideline value provides a practical reference point: the Ag^+ concentrations released from AgNP⊂SiO_2 monoliths in the present work (0.033–0.087 ppm in the 100× system at neutral pH) are well below this threshold, confirming the safety of the system for drinking water application under neutral conditions.

The European Union has not established a specific parametric value for silver in Directive 98/83/EC on the quality of water intended for human consumption,

applying instead the general principle that substances must not be present at concentrations that could constitute a danger to human health. For nanomaterials specifically, Commission Regulation (EU) No 10/2011 permits the use of certain nanoparticles (TiO_2, Si_3N_4, ZnO) in food-contact plastic materials only when used as embedded fillers from which nanoparticle migration is demonstrably impossible [15]. This regulatory philosophy — permitting nanoparticles only when their release into food or water is prevented — provides a clear design principle that the AgNP⊂SiO_2 monolith system satisfies by construction.

The European Food Safety Authority (EFSA) Panel on Food Additives and Nutrient Sources (ANS) issued a scientific opinion on silver as a food additive in 2018, concluding that the available data are insufficient to establish a safe level of oral AgNP exposure and recommending against their use as food additives [37]. The EFSA opinion explicitly distinguishes between ionic silver (Ag^+, for which limited toxicokinetic data exist) and nanoparticulate silver (AgNPs, for which systemic exposure and organ accumulation data are incomplete). This distinction reinforces the rationale for the present work: by permanently retaining AgNPs within the silica matrix and releasing only Ag^+ ions in controlled, sub-guideline quantities, the system sidesteps the principal regulatory uncertainty associated with AgNP ingestion.

Chapter 3. Materials and Methods

3.1 Chemicals and Materials

All chemicals were used as received without further purification. Silver nitrate ($AgNO_3$, ACS reagent, ≥99.0%), tannic acid (TA, ACS reagent), sodium citrate dihydrate (≥99.0%), N,N-dimethylformamide (DMF, >99.0%), tetramethyl orthosilicate (TMOS, ≥99.0%), methanol (HPLC grade, >99.9%), sodium hydroxide (≥98%), nitric acid (≥65%), and hydrochloric acid (≥37%) were purchased from Merck Life Science (Milano, Italy). Aqua regia ($HCl: HNO_3$ = 3:1 v/v) was prepared immediately before use. All glassware was treated with aqua regia for 15 min and washed three times with bidistilled water in an ultrasound bath (5 min each). Bidistilled water was used throughout.

3.2 Synthesis of Silver Nanoparticles

3.2.1 Reduction Mechanism

AgNPs were synthesized by a dual-reductant citrate–tannic acid method [16,17]. Tannic acid acts as the primary reducing agent: its phenolic hydroxyl groups donate electrons to Ag^+ ($Ag^+ + e^- \rightarrow Ag^0$), inducing an instantaneous burst of nucleation. Sodium citrate serves primarily as a stabilizing capping agent, adsorbing onto the AgNP surface and establishing a robust EDL preventing aggregation per DLVO theory [40].

3.2.2 Synthesis Procedure

A 50 mM sodium citrate solution and a 50 mM tannic acid solution were prepared separately in bidistilled water. In a three-neck round-bottom flask, 44 mL bidistilled water were combined with 5 mL citrate and 1 mL TA solutions under magnetic stirring. The mixture was heated to reflux (95–110 °C) with a

reflux condenser. Once at temperature, 1 mL of 25 mM $AgNO_3$ was rapidly injected (final Ag concentration: 4.9×10^{-4} M). An immediate yellow-orange color change confirmed AgNP formation. Heating was stopped and the mixture allowed to cool naturally to room temperature.

3.2.3 Purification and Concentration

The suspension was divided into five centrifuge tubes (10 mL each) and centrifuged at 12,000 RCF for 30 min. Three concentration levels were prepared: (i) 1×: each pellet redispersed in 10 mL of 2 mM citrate; (ii) 10×: all pellets combined in 5 mL of 2 mM citrate; (iii) 100×: the 10× sample centrifuged again (12,000 RCF, 30 min) and pellet redispersed in 0.5 mL of 2 mM citrate. The nominal Ag(0) concentrations of the 1×, 10×, and 100× suspensions are approximately 4.9×10^{-4} M, 4.9×10^{-3} M, and 4.9×10^{-2} M, respectively.

3.3 Preparation of Silica Monoliths

3.3.1 Sol–Gel Mechanism

TMOS undergoes base-catalyzed hydrolysis ($Si(OCH_3)_4 + 4\ H_2O \rightarrow Si(OH)_4 + 4\ CH_3OH$) followed by polycondensation ($\equiv Si–OH + HO–Si\equiv \rightarrow \equiv Si–O–Si\equiv + H_2O$) to build the siloxane network [22]. DMF was added as a DCCA to mitigate capillary stresses during drying ($\Delta P = 2\gamma\cos\theta/r$) and prevent crack formation [23].

3.3.2 Preparation Procedure

For AgNP-containing monoliths, 2.5 mL AgNP suspension (1×, 10×, or 100×) were mixed with 2.5 mL TMOS, 2.5 mL methanol, and 1.0 mL DMF under magnetic stirring until homogeneous. Then 100 µL of 0.05 M NaOH were added to initiate gelation. Stirring continued for exactly 5 min, then stopped. The sol was immediately cast into a 12-well plate (0.70 mL per well), sealed with Parafilm®, and left undisturbed for 3 days at 20 °C. Small holes were made in the Parafilm® for controlled evaporation, samples aged 3 further days, then dried

at 70 °C for 24 h to yield 1AgNP⊂SiO_2, 10AgNP⊂SiO_2, and 100AgNP⊂SiO_2. Plain silica controls were prepared identically with 2.5 mL bidistilled water.

3.4 Physicochemical Characterization

3.4.1 UV–Vis Absorption Spectroscopy

Spectra were recorded on a Varian Cary 60 spectrophotometer using 1 cm glass cuvettes for colloidal solutions or a dedicated solid sample holder for monoliths.

3.4.2 DLS and Zeta Potential

Hydrodynamic diameter and zeta potential were determined on a Zetasizer Ultra (Malvern Panalytical, 25 °C, 633 nm, 10 mW) in MADLS mode. Suspensions were diluted 1:10 (v/v) in water before analysis. Zeta potential was measured using a folded capillary cell (DTS1070) with the Hückel model. Three measurements per sample.

3.4.3 TEM

TEM imaging: JEOL JEM-1200 EX II, 100 kV. Samples (10 µL, 1:10 diluted) deposited on 300-mesh Ni grids with Parlodion membrane, dried overnight. Size analysis: 168 particles by Fiji/ImageJ automatic particle analysis (40 k×).

3.4.4 STEM-HAADF and EDS

Thermo Fisher Spectra 300 (300 kV, Cs probe corrector, 0.5 Å resolution, Super-X detector, ~0.8 sr). HAADF-STEM and EDS maps confirmed AgNP location and elemental distribution within the silica matrix.

3.4.5 XRPD

Bruker D6 diffractometer (Cu Kα, 40 mV, 15 mA, Ni filter, Bragg–Brentano geometry, 2θ = 10°–80°) on monolith samples on a zero-background Si holder.

3.4.6 TGA

Q5000 (TA Instruments): room temperature to 105 °C at 5 °C/min (30 min isotherm), then to 900 °C at 10 °C/min, under N_2 in a Pt pan.

3.5 Ag^+ Release Experiments

3.5.1 ISE Calibration

Ag^+ concentrations were determined using a Radiometer Analytical combined silver electrode (MC6091Ag-9) with Hg/Hg_2SO_4 reference electrode. The electrode follows the Nernst equation (theoretical slope 59.16 mV/decade at 25 °C, z = 1). Calibration was performed in the same background electrolyte as release experiments. Two calibration ranges were used (Table 3.1).

Concentration range (ppm)	Background electrolyte	Calibration equation	Slope (mV/dec)
0.1–100	0.1 M $NaNO_3$	$E = 236.23 + 54.76 \cdot \log[Ag^+]$	54.76
0.1–100	1.0 M $NaNO_3$	$E = 233.83 + 59.27 \cdot \log[Ag^+]$	59.27 (≈ Nernstian)
0.01–10	0.1 M $NaNO_3$	$E = 170.59 + 41.11 \cdot \log[Ag^+]$	41.11

Table 3.1. ISE calibration parameters for the two concentration ranges investigated.

3.5.2 Release Protocol

Baseline experiments: 0.1 M $NaNO_3$, room temperature, 10 mL per vial, one monolith per vial on reciprocating shaker. ISE readings at t = 0, 2, 5, 24, 72 h. All three loadings tested in duplicate. pH experiments: 100× monoliths in pH 4.0 and 5.5 (acetate buffer, 0.1 M) and pH 7.5 (HEPES, 0.1 M), at 5 h and 24 h. Temperature experiments: 100× monoliths in 0.1 M $NaNO_3$ at 37 °C in stoppered vial in oven, sampled at 5 h and 24 h.

3.5.3 ICP-OES Analysis

Total dissolved silver determined by ICP-OES (Perkin Elmer Optima 3300 DV). At each time point, 5.0 mL release medium were withdrawn, acidified with 0.1 mL concentrated HNO_3, diluted, and analyzed. ICP-OES detects all dissolved

silver species regardless of speciation, complementing the speciation-selective ISE.

3.6 Antimicrobial Activity Assay

3.6.1 Bacterial Strains and Inoculum

E. coli ATCC 10356 (Gram-negative) and S. aureus ATCC 6538 (Gram-positive) were grown overnight at 37 °C in TSB (Oxoid), centrifuged at 3,000 rpm for 20 min, resuspended in PBS (pH 7.4), and adjusted to A_{650} = 0.3 (~10^7–10^8 CFU/mL)[19].

3.6.2 Microbicidal Effect Protocol

One mL of bacterial suspension was added to 9 mL PBS in a Falcon tube containing one monolith (~100 mg). Incubation at 37 °C in a thermostatic shaking bath for 5 h and 24 h. Three parallel arms: (i) AgNP monoliths, (ii) plain silica blanks, (iii) inoculum control. After each contact time, serial dilutions were plated on TSA (Oxoid) and incubated at 37 °C for 24 h. The microbicidal effect was calculated as ME = $\log_{10}(CFU_{plain}) - \log_{10}(CFU_{a}{}^{\circ}{}_{np})$, and percentage reduction as $(1 - 10^{-ME}) \times 100$.

3.6.3 Tea-Bag Configuration

Monoliths were enclosed in double discs of filter paper (diameter 45 mm, pore size 0.45 μm) and placed into Falcon tubes with 10 mL bacterial suspension in PBS. Bacteria were exposed only to Ag^+ ions diffusing through the filter paper. The same ME protocol was applied.

Chapter 4. Results and Discussion

4.1 Synthesis and Characterization of Silver Nanoparticles

4.1.1 UV–Vis Spectroscopy

Formation of metallic AgNPs was confirmed by the immediate yellow-orange color change and by a well-defined LSPR band at λ_{max} = 422 nm (Figure 4.1B), characteristic of spheroidal AgNPs in the 30–40 nm range [4]. The band is sharp and symmetrical with no shoulders above 500 nm, confirming absence of significant aggregation. After incorporation into the silica matrix, the LSPR peak undergoes a bathochromic shift to 430 nm ($\Delta\lambda$ = 8 nm, Figure 4.1C), consistent with the higher refractive index of SiO_2 (n ≈ 1.46) vs. water (n = 1.33) per Mie theory, and confirms that no significant AgNP aggregation occurs during gelation.

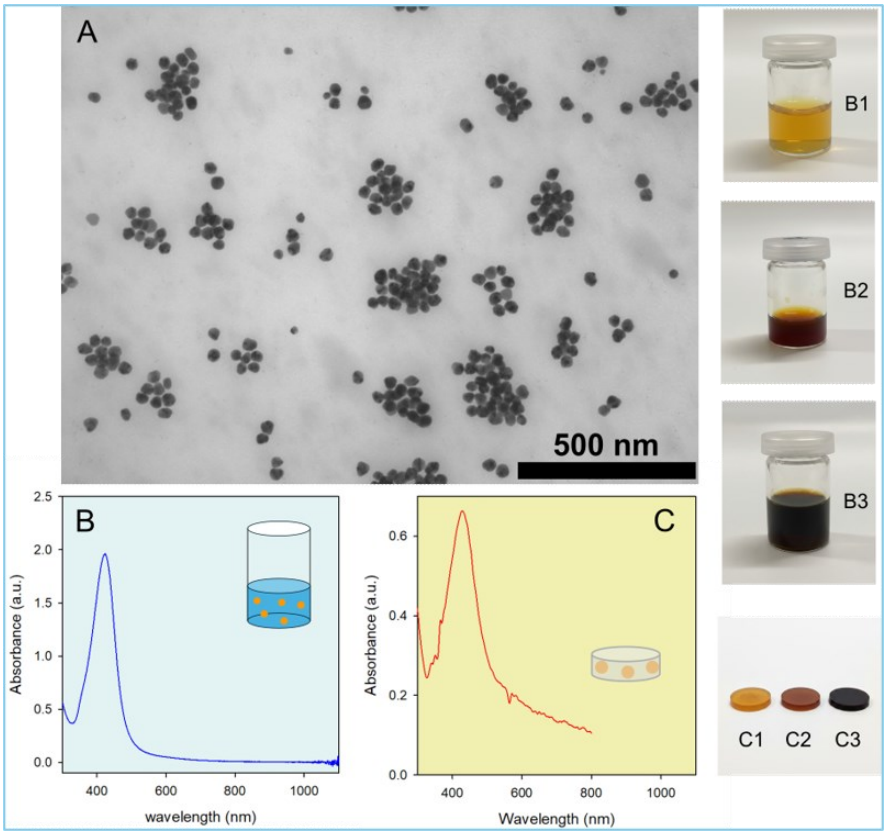

Figure 4.1. (A) TEM micrograph of AgNPs (scale bar 500 nm). (B) UV–Vis spectrum of 1× AgNP colloidal solution (LSPR at 422 nm). (B1–B3) Photographs of 1×, 10×, 100× AgNP suspensions. (C) UV–Vis spectrum of 1AgNP⊂SiO_2 monolith. (C1–C3) Photographs of 1×, 10×, 100× monoliths.

4.1.2 TEM Analysis

TEM analysis (Figure 4.1A) reveals well-dispersed spheroidal nanoparticles with a mean core diameter of 36.1 ± 6.5 nm (168 particles, Fiji/ImageJ). The narrow size distribution and absence of aggregates confirm effective stabilization by the citrate–tannic acid capping shell.

4.1.3 DLS and Zeta Potential

DLS on the optimized batch gave Z-average = 44.86 ± 0.48 nm and PDI = 0.176 ± 0.004 (Table 4.1), confirming a monodisperse system. The ~9 nm difference between hydrodynamic and TEM diameters reflects the adsorbed capping layer and hydration shell. Zeta potential = −31.67 ± 2.5 mV confirms excellent colloidal stability, exceeding the −30 mV DLVO threshold [40].

Parameter	Batch 0403 (initial)	Batch 0703 (optimized)
Z-average diameter (nm)	52.7	44.86 ± 0.48
PDI	0.220	0.176 ± 0.004
Number mean (nm)	—	36.96
Intensity mean (nm)	—	52.50
Zeta potential (mV)	—	−31.67 ± 2.5
TEM core diameter (nm)	—	36.1 ± 6.5

Table 4.1. Physicochemical characterization of AgNP batches (mean of three independent measurements).

4.2 Characterization of AgNP⊂SiO_2 Monoliths

4.2.1 SEM

SEM at 100 k× of the 100AgNP⊂SiO_2 monolith surface (both upper and lower sides) reveals a uniformly granular silica texture with no visible AgNPs (Figure 4.3), confirming that nanoparticles are distributed throughout the silica bulk and absent from the external surface. This eliminates the risk of mechanical detachment of intact nanoparticles into treated water.

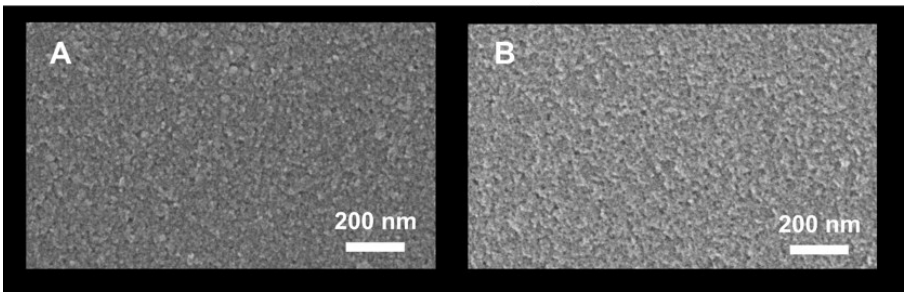

Figure 4.3. SEM images (100 k×) of the upper (A) and lower (B) surface of 100AgNP⊂SiO_2. No AgNPs are visible on either surface.

4.2.2 STEM-HAADF and EDS

HAADF-STEM (Figure 4.4A) reveals bright circular spots of ~40 nm consistent with AgNPs (Z^2 contrast: $Z_a^2 = 47$ vs. $Z_s^I = 14$). EDS maps confirm: Ag (Figure 4.4C, discrete spots co-localizing with HAADF features), Si and O (Figures 4.4D and B, continuous distribution). Together, SEM and STEM-EDS establish that

AgNPs are embedded within the silica body and inaccessible from the external surface.

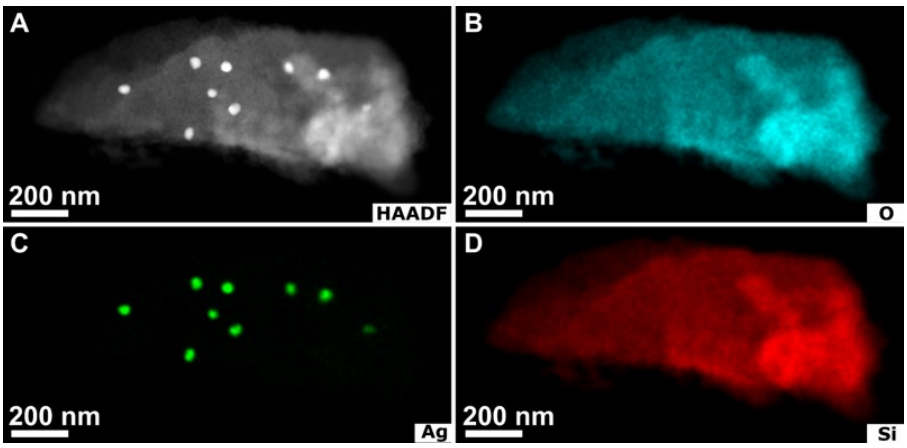

Figure 4.4. STEM-HAADF (A) and EDS elemental maps of O (B, cyan), Ag (C, green), Si (D, red) for 100AgNP⊂SiO_2. Bright spots in (A) are ~40 nm AgNPs embedded within the silica matrix.

4.2.3 XRPD

The XRPD pattern (Figure 4.5) shows a broad amorphous halo at 2θ ≈ 22° (amorphous SiO_2) with four peaks at 38.09° (111), 44.27° (200), 64.43° (220), and 76.43° (311) corresponding to fcc metallic Ag (JCPDS 04-0783) [31]. Low peak intensity is consistent with small crystallites embedded under amorphous silica, confirming Ag^0 within the monolith.

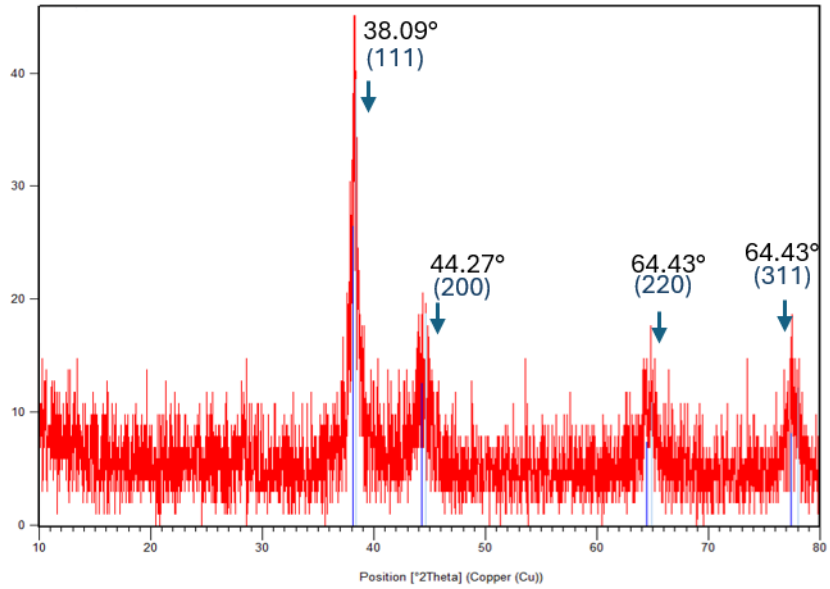

Figure 4.5. XRPD pattern of 100AgNP⊂SiO₂ (Cu Kα). Broad halo at ~22°: amorphous SiO₂. Peaks at 38.09°, 44.27°, 64.43°, 76.43°: fcc Ag⁰ (hkl planes labeled).

4.2.4 Total Silver Content of the Monoliths

The nominal total Ag(0) content in a single monolith was calculated from the concentration of AgNPs in the precursor sol and the volume cast per well (0.70 mL), assuming quantitative retention during gelation. The actual Ag(0) content was verified by complete dissolution in concentrated HNO_3 followed by ICP-OES analysis, yielding 95–100% of the nominal values in all cases (Table 4.2).

Monolith	Total Ag[a](nominal, µg)	Available Silver Concentration ASC[b] (µg/mL)	Ag^+ release at 24 h (% of total Ag)[c]
1AgNP⊂SiO_2	10.9	1.09	0.71%
10AgNP⊂SiO_2	109	10.9	0.12%
100AgNP⊂SiO_2	1090	109	0.060%

Table 4.2. Total Ag[a] content and Available Silver Concentration (ASC) of AgNP⊂SiO₂ monoliths. [b]ASC is the Available Silver Concentration = total nominal Ag in a monolith/10 mL. [c]Percentage of total Ag content released into 10 mL bidistilled water at 20 °C after 24 h, measured by ICP-OES.

These data highlight a key feature of the AgNP⊂SiO_2 system: only a very small fraction of the total silver content is released at any given time point. At 24 h,

the 100× monolith releases only 0.060% of its total Ag content, corresponding to 0.065 ppm in 10 mL. This controlled, limited release is essential for sustained long-term efficacy and for maintaining Ag^+ concentrations below the WHO guideline value of 0.1 mg/L. The low % release also suggests that these monoliths could remain active over many disinfection cycles before depletion of their silver content.

4.3 Ag^+ Release Studies

4.3.1 Effect of AgNP Loading

All three loadings display a biphasic release profile: a faster initial phase within 2–5 h followed by slower sustained release (Figure 4.6), characteristic of diffusion-controlled ion transport through the silica pore network [27]. Ag^+ release increases sub-linearly with loading: a 100-fold increase in AgNP content yields only ~3-fold increase at 24 h (Table 4.3), reflecting steric constraints on nanoparticle accessibility within the dense silica interior.

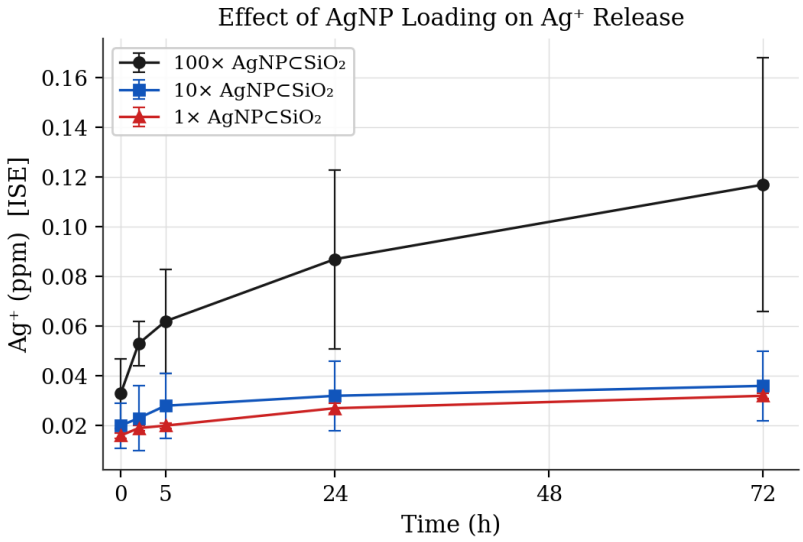

Figure 4.6. ISE kinetics of Ag^+ release from 1×, 10×, and 100× AgNP⊂SiO_2 monoliths in 0.1 M $NaNO_3$ at room temperature over 72 h. Error bars represent the standard deviation of duplicate measurements.

Monolith	ISE 5 h (ppm)	ISE 24 h (ppm)	ICP-OES 5 h (ppm)	ICP-OES 24 h (ppm)
1× AgNP⊂SiO_2	0.020 ± 0.001	0.027 ± 0.002	0.001 ± 0.001	0.008 ± 0.003
10× AgNP⊂SiO_2	0.028 ± 0.001	0.032 ± 0.001	0.005 ± 0.003	0.013 ± 0.001
100× AgNP⊂SiO_2	0.062 ± 0.021	0.087 ± 0.036	0.053 ± 0.022	0.065 ± 0.028

Table 4.3. Ag^+ release from AgNP⊂SiO_2 monoliths at different loadings in 0.1 M $NaNO_3$ (ISE) and bidistilled water (ICP-OES), room temperature.

4.3.2 Effect of pH

A strong and systematic pH dependence is observed (Figure 4.7, Figure 4.8, Table 4.3), consistent with reaction (1.1): lower pH shifts equilibrium toward Ag^+ formation [26]. At pH 4.0, the 24 h ICP-OES value reaches 0.621 ppm, approximately ten times higher than at pH 7.5 (0.054 ppm). ISE values are consistently lower than ICP-OES at acidic pH, reflecting formation of silver–acetate complexes undetectable by the ISE.

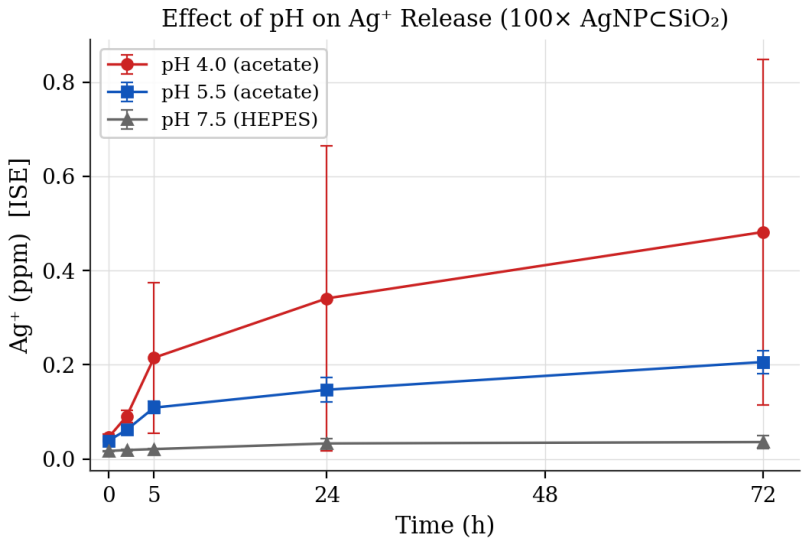

Figure 4.7. ISE kinetics of Ag^+ release from 100× AgNP⊂SiO_2 at pH 4.0, 5.5, and 7.5 (room temperature, 72 h).

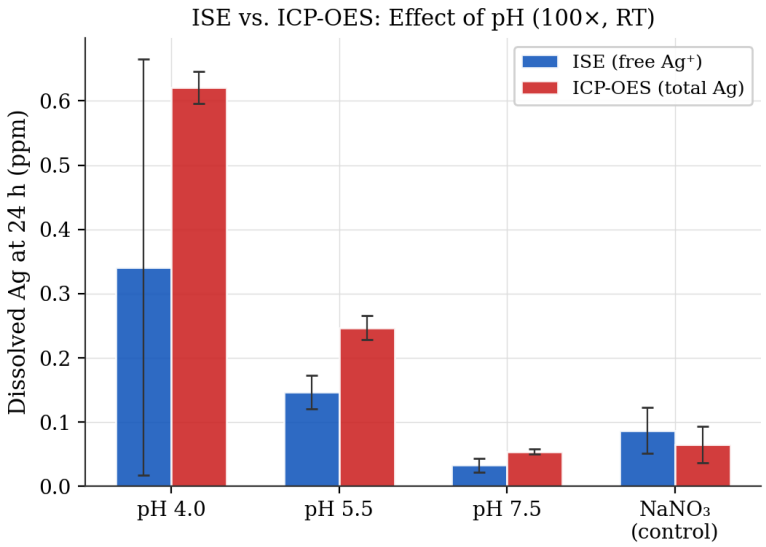

Figure 4.8. ISE (free Ag^+) vs. ICP-OES (total dissolved Ag) at 24 h under different pH conditions. Divergence reflects silver–acetate complex formation at acidic pH.

Medium	ISE 5 h (ppm)	ISE 24 h (ppm)	ICP-OES 5 h (ppm)	ICP-OES 24 h (ppm)
pH 4.0 (acetate)	0.215 ± 0.160	0.341 ± 0.324	0.289 ± 0.121	0.621 ± 0.025
pH 5.5 (acetate)	0.109 ± 0.013	0.147 ± 0.026	0.125 ± 0.063	0.247 ± 0.019
pH 7.5 (HEPES)	0.021 ± 0.001	0.033 ± 0.011	0.047 ± 0.044	0.054 ± 0.004
0.1 M $NaNO_3$	0.062 ± 0.021	0.087 ± 0.036	0.053 ± 0.022	0.065 ± 0.028

Table 4.4. Effect of pH on Ag^+ release from 100× AgNP⊂SiO_2, room temperature.

4.3.3 Effect of Temperature

Release at 37 °C yields approximately twofold higher total dissolved silver at 24 h vs. room temperature (0.170 vs. 0.065 ppm by ICP-OES, Table 4.4, Figure 4.9), reflecting Arrhenius-type kinetic acceleration and the thermodynamic decrease in Ag^+/Ag^0 reduction potential with temperature [26].

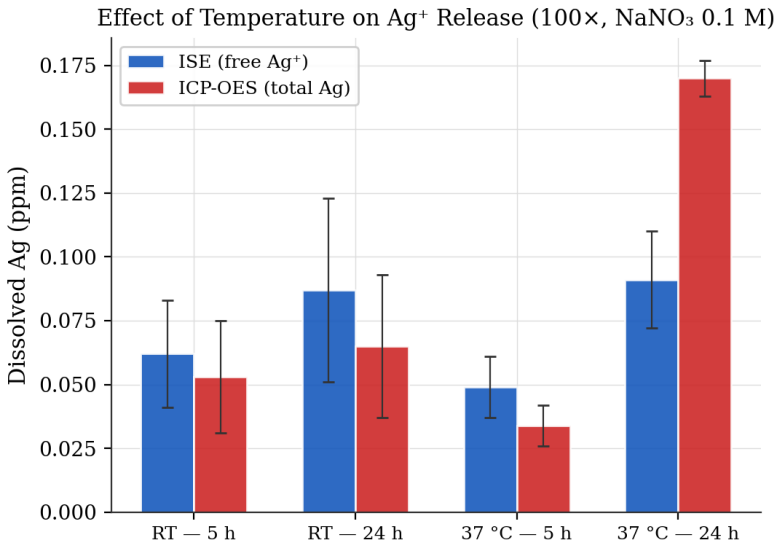

Figure 4.9. Effect of temperature on Ag^+ release from 100× $AgNP \subset SiO_2$ in 0.1 M $NaNO_3$, measured by ISE and ICP-OES at 5 h and 24 h.

Temperature	ISE 5 h (ppm)	ISE 24 h (ppm)	ICP-OES 5 h (ppm)	ICP-OES 24 h (ppm)
Room temp. (~20 °C)	0.062 ± 0.021	0.087 ± 0.036	0.053 ± 0.022	0.065 ± 0.028
37 °C	0.049 ± 0.012	0.091 ± 0.019	0.034 ± 0.008	0.170 ± 0.007

Table 4.5. Effect of temperature on Ag^+ release from 100× $AgNP \subset SiO_2$ in 0.1 M $NaNO_3$.

4.3.4 ISE vs. ICP-OES: Silver Speciation

The ISE responds exclusively to free, uncomplexed $Ag^+(aq)$. Silver–acetate complexes at pH 4.0–5.5 and silver–chloro complexes in PBS (($[AgCl_2]^-$, $[AgCl_3]^{2-}$) [28] are invisible to the ISE but fully detected by ICP-OES. In PBS (140 mM Cl^-), ISE readings approach zero while ICP-OES confirms continuous silver release. These chlorocomplexes retain antimicrobial activity through passive diffusion via bacterial outer membrane porins, followed by intracellular Ag^+ release upon dissociation [29].

4.3.5 Percentage of Total Silver Released

A key performance metric for any silver-based disinfection device is what fraction of the total silver reservoir is consumed per use cycle. Table 4.7 reports

the percentage of total Ag(0) released as Ag^+ at 5 h and 24 h, calculated from the ICP-OES values in Table 4.3 and the total Ag content in Table 4.2, for experiments carried out in bidistilled water at 20 °C according to equation 4.1:

$$\% \text{ Ag released} = (C_a{}^{a} \text{ [ppm]} \times V \text{ [L]} / M^{Tot}{}_{al} \text{ [mg]}) \times 100 \quad (4.1)$$

where $C_a{}^{a}$ is the ICP-OES concentration (ppm = mg/L), V is the volume of water (0.010 L), and $M^{Tot}{}_{al}$ is the total nominal Ag(0) content of the monolith (mg).

Monolith	Total Ag^T (µg)	ICP-OES 5 h (ppm)	Ag released 5 h (µg)	% released 5 h	ICP-OES 24 h (ppm)	Ag released 24 h (µg)	% released 24 h
1× AgNP⊂SiO_2	10.9	0.001	0.010	0.0009%	0.008	0.080	0.073%
10× AgNP⊂SiO_2	109	0.005	0.050	0.0005%	0.013	0.130	0.012%
100× AgNP⊂SiO_2	1090	0.053	0.530	0.0005%	0.065	0.650	0.006%

Table 4.7. Percentage of total Ag (0) content released as Ag^+ from AgNP⊂SiO_2 monoliths in 10 mL bidistilled water at 20 °C, measured by ICP-OES. [T]Total nominal Ag (0) content per monolith (from Table 4.2). [b]

These data reveal a striking feature of the AgNP⊂SiO_2 system: the fraction of total silver released at 24 h is remarkably small, ranging from 0.006% (100×) to 0.073% (1×). This sub-0.1% release at neutral pH has two important practical implications.

First, the released Ag^+ concentrations are sufficient for effective bacterial inactivation (>99% CFU reduction at 24 h, Table 4.6) while remaining well below the WHO guideline value of 0.1 mg/L for silver in drinking water [2] under neutral and near-neutral conditions. For the 100× monolith in bidistilled water at 24 h, the ICP-OES value is 0.065 ppm — below the WHO limit; even at 37 °C the release reaches 0.170 ppm, still at the same order of magnitude as the guideline value.

Second, the vast reservoir of unreleased Ag(0) within the monolith ensures a prolonged operational lifetime. Taking the 100× monolith as an example: with a total Ag content of 1090 mg and releasing only 0.65 µg per 24 h cycle (0.006% per cycle), the theoretical number of disinfection cycles before full depletion exceeds 1.6×10^6, assuming constant release rate. Even accounting for any increase in release rate over extended time, these numbers confirm that the AgNP⊂SiO_2 monolith functions as an essentially inexhaustible silver reservoir for practical POU applications. This is fully consistent with the values reported in Table 1 of the submitted manuscript, which shows that only 0.006–0.073% of the total Ag content is released after 24 h in bidistilled water at 20 °C.

4.4 Antimicrobial Activity

4.4.1 Microbicidal Effect

All three loadings achieved ME > 1.95 against both organisms at 5 h, increasing to ME > 2.42 at 24 h (>99% CFU reduction, Table 4.5). At 24 h with 100×, ME = 4.07 against E. coli (>99.99%) and ME = 2.65 against S. aureus (~99.78%).

Bacterium	Monolith	ME at 5 h	ME at 24 h	CFU reduction at 24 h (%)
E. coli	1×	0.6	2.42	>99.62
E. coli	10×	3.7	3.69	>99.98
E. coli	100×	3.4	4.07	>99.99
S. aureus	1×	2.0	1.95	98.88
S. aureus	10×	1.8	2.41	99.61
S. aureus	100×	2.0	2.65	99.78

Table 4.6. Microbicidal effect (ME) of AgNP⊂SiO_2 monoliths against E. coli and S. aureus at 5 h and 24 h in PBS at 37 °C.

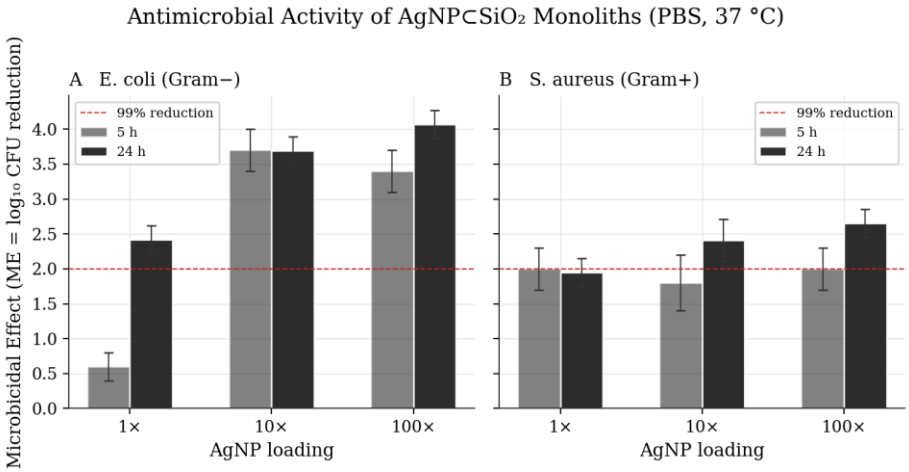

Figure 4.10. Microbicidal effect of AgNP⊂SiO₂ monoliths. (A) E. coli (Gram−); (B) S. aureus (Gram+). Dark bars: 24 h; light bars: 5 h. Dashed line: ME = 2 (99% CFU reduction threshold).

4.4.2 Gram-Positive vs. Gram-Negative Susceptibility

E. coli consistently shows higher ME values than *S. aureus*. *E. coli* possesses a thin peptidoglycan layer (2–3 nm) beneath an outer membrane bearing porin channels that facilitate Ag^+ entry. *S. aureus* presents a thick, cross-linked peptidoglycan meshwork (30–80 nm) enriched in teichoic and lipoteichoic acids, acting as an electrostatic sink for Ag^+ and creating a diffusion barrier that attenuates intracellular silver delivery [30].

4.4.3 Tea-Bag Configuration

At 5 h, the tea-bag configuration shows reduced ME values due to additional mass-transfer resistance from the filter paper layer. By 24 h, ME values converge with those of free monoliths for all conditions tested (Figure 4.11), confirming that the filter paper does not significantly limit Ag^+ transport at equilibrium.

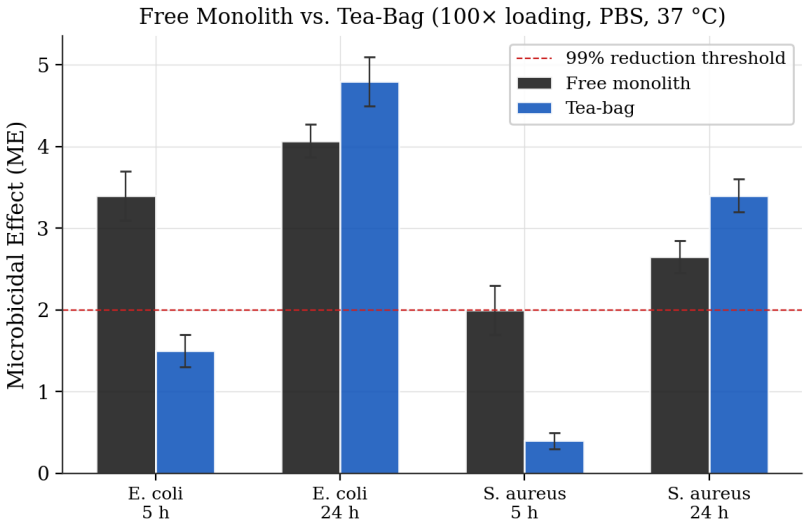

Figure 4.11. Free monolith vs. tea-bag configuration (100×) against E. coli and S. aureus at 5 h and 24 h in PBS at 37 °C. Dashed line: ME = 2 (99% CFU reduction threshold).

Chapter 5. Conclusions and Future Perspectives

5.1 Summary of Principal Findings

This thesis has demonstrated the feasibility and efficacy of macroscopic silica monoliths with physically embedded silver nanoparticles (AgNP⊂SiO_2) as a platform for safe, sustained-release point-of-use water disinfection.

(i) AgNPs with controlled size (36.2 ± 6.5 nm by TEM, Z-average 44.86 nm), narrow size distribution (PDI 0.176), and excellent colloidal stability (zeta potential −31.67 mV) were reproducibly synthesized by dual-reductant citrate–tannic acid co-reduction [16,17].

(ii) AgNP⊂SiO_2 monoliths at three loadings (1×, 10×, 100×, corresponding to a total of 10.9, 109, and 1090 Ag micrograms per single monolith, respectively) were prepared by TMOS sol–gel. SEM confirmed absence of AgNPs on the surface; STEM-EDS demonstrated embedding within the bulk; XRPD confirmed fcc Ag^0; LSPR redshift (422→430 nm) confirmed encapsulation without aggregation.

(iii) Ag^+ release follows a diffusion-controlled, sustained-release profile. Release increases sub-linearly with loading. Crucially, only a very small percentage of the total silver contained within the monoliths is released at 5 h and 24 h (ranging from 0.060% to 0.71% of the total Ag content at 24 h) is expected to provide a long operational lifetime before depletion. Strong pH dependence was observed (pH 4.0: 0.621 ppm vs. pH 7.4: 0.054 ppm by ICP-OES at 24 h). Temperature elevation to 37 °C approximately doubled the 24 h ICP-OES value.

(iv) ISE–ICP discrepancies demonstrated silver speciation: silver–acetate complexes at acidic pH are detected by ICP-OES but not by the ISE. In PBS (140 mM Cl^-), total dissolved silver was below the ICP-OES detection limit due to AgCl precipitation and speciation; yet the strong antimicrobial activity confirms a continuous micro-flux of bioavailable silver chloro-complexes ($[AgCl_2]^-$) that are believed to remain microbiologically active.

(v) All three loadings achieved >99% CFU reduction of both *E. coli* and *S. aureus* after 24 h at 37 °C in PBS (100×: ME = 4.07 vs. *E. coli*, ME = 2.65 vs. *S. aureus*). Lower *S. aureus* susceptibility reflects its thick polyanionic peptidoglycan wall acting as an electrostatic Ag^+ sink.

(vi) The tea-bag configuration achieved equivalent 24 h antimicrobial performance, demonstrating practical feasibility for on-demand POU disinfection without direct monolith–water contact.

5.2 Significance and Broader Implications

The AgNP⊂SiO_2 platform addresses the critical nanopollution limitation of surface-decorated materials by achieving physical size exclusion of nanoparticles while maintaining Ag^+ diffusion. This is aligned with EU regulatory principles [15] requiring that nanoparticles in food/water-contact applications not migrate into the product. The tea-bag format requires no electricity, no technical expertise, and no specialized equipment, making it directly applicable to resource-limited settings and emergency response scenarios. Significantly, the released Ag^+ remains under the allowed limit set by the World Health Organization of 0.1 mg/L (0.1 ppm) for drinking water.

The combined use of ISE and ICP-OES as complementary analytical tools provided mechanistic insight not achievable by either technique alone,

demonstrating that silver speciation in complex matrices does not compromise antimicrobial efficacy, because soluble silver complexes maintain bioavailability through alternative uptake pathways.

5.3 Limitations

All antimicrobial experiments were conducted in PBS rather than natural water matrices, which contain natural organic matter, humic substances, and dissolved ions that may bind Ag^+. Long-term reusability over multiple disinfection cycles has not been systematically assessed. Concentration techniques (e.g., ultrafiltration) coupled with UV-Vis absorption spectroscopy would be advisable for the verification of possible trace release of Ag nanoparticles.

5.4 Future Research Directions

(i) Natural water testing. Evaluate efficacy and Ag^+ release kinetics in natural water samples of varying hardness, organic content, and microbial load.

(ii) Long-term reusability. Systematic assessment over 10–50 disinfection cycles to establish operational lifetime and AgNP depletion rate.

(iii) Virus and protozoan inactivation. Extend evaluation to MS2 bacteriophage and Cryptosporidium to broaden the demonstrated scope.

(iv) Nanoparticle release quantification. Concentration and UV-Vis absorption spectra to provide definitive evidence that AgNP release negligible/null.

(v) Visible-light photocatalytic extension. Integration of Ag/TiO_2 nanocomposites into the sol–gel matrix to enable simultaneous photocatalytic degradation of organic micropollutants (antibiotics, hormones, NSAIDs) via SPR-driven ROS generation.

5.5 Graphical Summary

Figure 5.1 provides a visual overview of the complete workflow presented in this thesis, from AgNP synthesis to the final antimicrobial application, including key molecular structures, the sol–gel encapsulation strategy, Ag^{+} release mechanism, and differential antibacterial response.

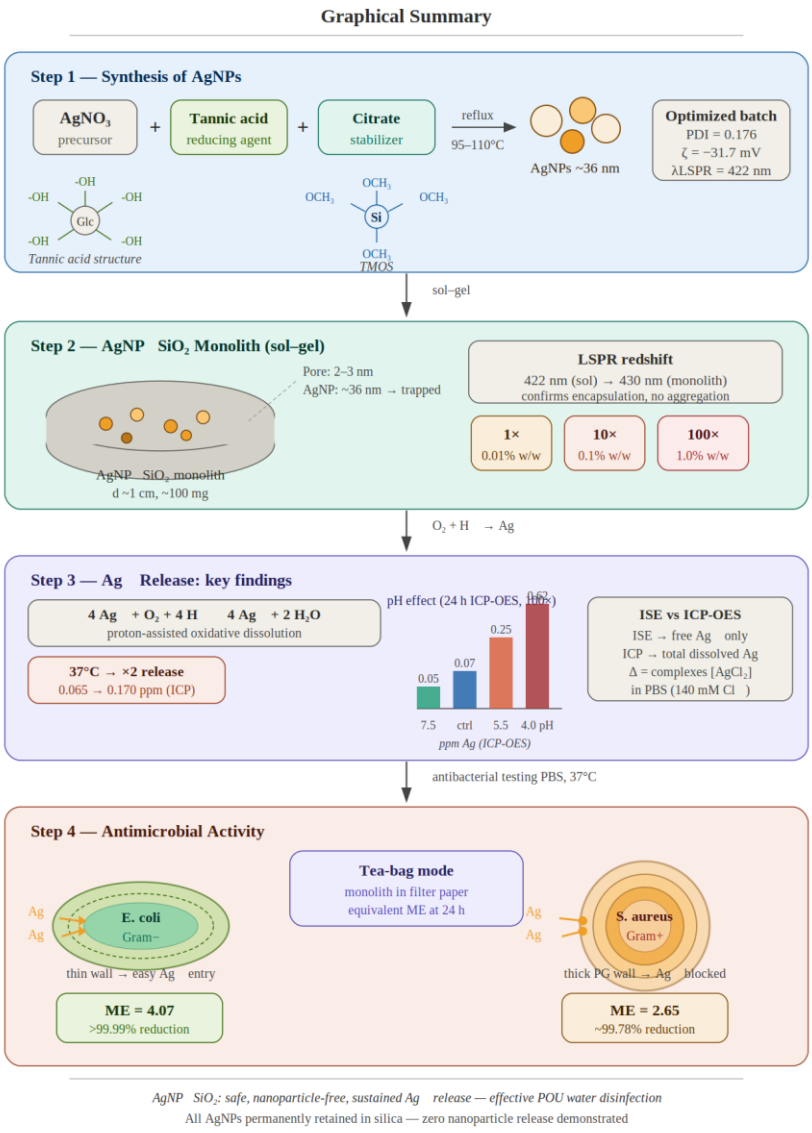

Figure 5.1. Graphical summary of the thesis. Step 1: AgNP synthesis via citrate–tannic acid co-reduction (molecular structures of TA and TMOS shown). Step 2: AgNP⊂SiO_2 monolith by TMOS sol–gel; pore diameter 2–3 nm traps AgNPs (~36 nm) while allowing Ag^+ diffusion. Step 3: release is pH- and temperature-dependent; ISE/ICP-OES discrepancy reflects silver speciation. Step 4: E. coli (ME = 4.07, >99.99%) and S. aureus (ME = 2.65, ~99.78%); tea-bag mode achieves equivalent 24 h performance.

Chapter Appendix. undefined

Appendix A — ISE Calibration Procedure and Curves

The Ag^+ concentration in all release experiments was determined using a Radiometer Analytical combined silver electrode (model MC6091Ag-9) with a Hg/Hg_2SO_4 reference electrode. Calibration was performed prior to each set of measurements using serial dilutions of $AgNO_3$ stock solution in the same background electrolyte as the release experiments, to maintain constant ionic strength.

Two independent calibration ranges were established (Tables A.1 and A.2). The linear regression equations are:

$$0.1\ M\ NaNO_3: \quad E = 236.23 + 54.76 \cdot \log[Ag^+] \quad (R^2 = 0.9981)$$

$$1.0\ M\ NaNO_3: \quad E = 233.83 + 59.27 \cdot \log[Ag^+] \quad (R^2 = 0.9994)$$

Ag^+ (ppm)	$\log[Ag^+]$	E (mV) — 0.1 M $NaNO_3$	E (mV) — 1.0 M $NaNO_3$
0.1	−1.000	−82.3	−123.0
0.2	−0.699	−74.7	−105.5
0.5	−0.301	−59.4	−89.0
1.0	0.000	−45.2	−69.5
2.0	0.301	−31.0	−42.5
5.0	0.699	−6.3	−20.0
10.0	1.000	16.8	−4.3
20.0	1.301	36.5	12.9
50.0	1.699	54.3	35.3
100.0	2.000	76.7	50.5

Table A.1. ISE calibration data for the high-concentration range (0.1–100 ppm Ag^+) in 0.1 M and 1.0 M $NaNO_3$.

Ag^+ (ppm)	log[Ag^+]	E (mV) — 0.1 M $NaNO_3$
0.01	−2.000	−109.0
0.02	−1.699	−103.0
0.05	−1.301	−95.0
0.1	−1.000	−84.5
0.2	−0.699	−68.5
0.5	−0.301	−49.5
1.0	0.000	−37.7
2.0	0.301	−25.5
5.0	0.699	−4.0
10.0	1.000	9.8

Table A.2. ISE calibration data for the low-concentration range (0.01–10 ppm Ag^+) in 0.1 M $NaNO_3$. Slope = 41.11 mV/decade (sub-Nernstian, R^2 = 0.9921).

Appendix B — Complete Raw ISE and ICP-OES Release Data

Tables B.1–B.5 report the complete raw datasets from all Ag^+ release experiments, including electrode potential readings (E, mV), calculated Ag^+ concentrations by ISE (ppm), and total dissolved silver by ICP-OES (ppm), together with standard deviations (SD) and relative standard deviations (RSD%).

Time	t (min)	E^{mem} (mV)	SD^{ILL} (mV)	$[Ag^+]$ ISE (ppm)	ICP-OES (ppm)	SD ICP (ppm)
0 h	0	−120.3	±9.50	0.033	—	—
2 h	120	−109.3	±3.79	0.053	—	—
5 h	300	−105.5	±6.11	0.062	0.053	±0.022
24 h	1440	−97.5	±7.64	0.087	0.065	±0.028
72 h	4320	−90.3	±9.29	0.117	—	—

Table B.1. Complete ISE and ICP-OES data for 100× AgNP⊂SiO_2 in 0.1 M $NaNO_3$, room temperature.

Condition	Time	E^{mem} (mV)	SD^{ILL} (mV)	$[Ag^+]$ ISE (ppm)	ICP-OES (ppm)	SD ICP (ppm)
pH 4.0	5 h	−76.0	±16.97	0.215	0.289	±0.121
pH 4.0	24 h	−65.0	±21.21	0.341	0.621	±0.025
pH 5.5	5 h	−92.0	±2.83	0.109	0.125	±0.063
pH 5.5	24 h	−85.0	±4.24	0.147	0.247	±0.019
pH 7.4	5 h	−131.0	±3.61	0.021	0.047	±0.044
pH 7.4	24 h	−120.3	±5.51	0.033	0.054	±0.004
Bidist. water	5 h	−105.5	±6.11	0.062	0.053	±0.022
Bidist. water	24 h	−97.5	±7.64	0.087	0.065	±0.028

Table B.2. Complete ISE and ICP-OES data for 100× AgNP⊂SiO_2 at different pH values and in bidistilled water, room temperature.

Temperature	Time	E^{mem} (mV)	SD^{ILL} (mV)	$[Ag^+]$ ISE (ppm)	ICP-OES (ppm)	SD ICP (ppm)
Room temp.	5 h	−105.5	±6.11	0.062	0.053	±0.022
Room temp.	24 h	−97.5	±7.64	0.087	0.065	±0.028
37 °C	5 h	−111.0	±5.66	0.049	0.034	±0.008

Temperature	Time	E^{mem} (mV)	SD^{ILL} (mV)	[Ag^+] ISE (ppm)	ICP-OES (ppm)	SD ICP (ppm)
37 °C	24 h	−96.5	±4.95	0.091	0.170	±0.007

Table B.3. Complete ISE and ICP-OES data for 100× AgNP⊂SiO_2 at room temperature and 37 °C in 0.1 M $NaNO_3$.

Appendix C — ICP-OES Data for PBS Buffer Experiments

Release experiments were also performed in phosphate-buffered saline (PBS, pH 7.4, 140 mM Cl^-) to replicate the conditions of the antimicrobial activity assay. In this medium, Ag^+ ions are quantitatively converted to soluble silver–chloro complexes ($[AgCl_2]^-$, $[AgCl_3]^{2-}$), rendering the ISE signal near-zero (see Section 4.3.4). Therefore, total dissolved silver was quantified exclusively by ICP-OES.

Sample label	ICP-OES raw (ppm)	Blank average (ppm)	Corrected value (ppm)
100× PBS — 5 h	−0.01134	−0.00446	−0.00688 (≈ 0)*
100× PBS — 24 h	−0.00367	−0.00446	0.00079 (≈ 0)*
Blank control 1	−0.007	—	—
Blank control 2	−0.010	—	—
Blank control 3	−0.011	—	—
Blank control 4	0.011	—	—
Blank average	−0.00446	—	—

Table C.1. ICP-OES results for 100× AgNP⊂SiO_2 monoliths in PBS (pH 7.4). All values are below or at the instrument detection limit after blank correction (*). The near-zero ICP-OES signal is consistent with rapid conversion of Ag^+ to insoluble AgCl precipitate and/or soluble chlorocomplexes that are present at concentrations below the ICP-OES detection limit in this matrix.

The near-zero ICP-OES values in PBS are consistent with the known solution chemistry of silver in high-chloride media. At 140 mM Cl^- (the physiological chloride concentration in PBS), the initial Ag^+ released from the monolith is quantitatively precipitated as AgCl (K_{sp} = 1.77 × 10^{-10}) and/or converted to soluble anionic chlorocomplexes ($[AgCl_2]^-$, $\beta_2 \approx 2.5 \times 10^5$; $[AgCl_3]^{2-}$, $\beta_3 \approx 2.0 \times 10^5$). The total dissolved silver concentration in PBS is therefore below the ICP-OES detection limit under the experimental conditions used, while the antimicrobial efficacy (ME > 2 for all loadings) confirms that bioavailable silver species are indeed delivered to the bacterial cells.

These results are fully consistent with the mechanistic interpretation presented in Section 4.3.4: the antimicrobial activity in PBS is mediated by neutral AgCl(aq) and anionic chlorocomplexes that diffuse passively through bacterial outer membrane porins, releasing Ag^+ intracellularly upon dissociation in the low-chloride cytoplasm.

References

All references are numbered consecutively in order of first appearance in the text. References appearing in Chapter 1 are numbered [1]–[13]; those first appearing in Chapter 2 continue from [14]; and so on.

[1] Dutta, T.; Barman, A.; Bhattacherjee, S.; Chakraborty, J.; Dutta, T. Antimicrobial silver nanoparticles for water disinfection: a short review on recent advances. Nanotechnology. Environ. Eng. 2024, 9, 111–131. DOI: 10.1007/s41204-023-00354-5

[2] World Health Organization. Guidelines for Drinking-Water Quality, 4th edition incorporating the 1st and 2nd addenda; WHO Press: Geneva, 2011; pp 128–129.

[3] World Health Organization. Alternative Drinking-Water Disinfectants: Bromine, Iodine and Silver; WHO: Geneva, 2018. Licence: CC BY-NC-SA 3.0 IGO.

[4] Zheng, K.; Setyawati, M. I.; Leong, D. T.; Xie, J. Antimicrobial silver nanomaterials. Coord. Chem. Rev. 2018, 357, 1–17. DOI: 10.1016/j.ccr.2017.11.019

[5] Dankovich, T. A.; Gray, G. G. Bactericidal paper impregnated with silver nanoparticles for point-of-use water treatment. Environ. Sci. Technol. 2011, 45, 1992–1998. DOI: 10.1021/es103302t

[6] Mecha, C.; Pillay, V. L. Development and evaluation of woven fabric microfiltration membranes impregnated with silver nanoparticles for potable water treatment. J. Membr. Sci. 2014, 458, 149–156. DOI: 10.1016/j.memsci.2014.02.001

[7] Oyanedel-Craver, V. A.; Smith, J. A. Sustainable colloidal-silver-impregnated ceramic filter for point-of-use water treatment. Environ. Sci. Technol. 2008, 42, 927–933. DOI: 10.1021/es071268u

[8] Kallman, E. N.; Oyanedel-Craver, V. A.; Smith, J. A. Ceramic filters impregnated with silver nanoparticles for point-of-use water treatment in rural Guatemala. J. Environ. Eng. 2011, 137, 407–415. DOI: 10.1061/(ASCE)EE.1943-7870.0000330

[9] Mthombeni, N. H.; Mpenyana-Monyatsi, L.; Onyango, M. S.; Momba, M. N. Breakthrough analysis for water disinfection using silver nanoparticles coated resin beads in fixed-bed column. J. Hazard. Mater. 2012, 217, 133–140. DOI: 10.1016/j.jhazmat.2012.03.004

[10] Jiang, S.; Tang, C.; Gong, Z.; Zhang, Z.; Wang, D.; Fan, M. Facile preparation of chitosan coated silver nanoparticles embedded cotton fabric for point-of-use water disinfection. Mater. Lett. 2020, 277, 128256. DOI: 10.1016/j.matlet.2020.128256

[11] Tessema, B.; Gonfa, G.; Hailegiorgis, S. M. Synthesis of modified silica gel supported silver nanoparticles for the application of drinking water disinfection: a review. Res. Eng. 2024, 22, 102261. DOI: 10.1016/j.rineng.2024.102261

[12] Borzenkov, M.; Pallavicini, P.; Taglietti, A.; D'Alfonso, L.; Collini, M.; Chirico, G. Photothermally active nanoparticles as a promising tool for eliminating bacteria and biofilms. Beilstein J. Nanotechnol. 2020, 11, 1134–1146. DOI: 10.3762/bjnano.11.98

[13] Pallavicini, P.; Dacarro, G.; Taglietti, A. Self-assembled monolayers of silver nanoparticles: from intrinsic to switchable inorganic antibacterial surfaces. Eur. J. Inorg. Chem. 2018, 4846–4855. DOI: 10.1002/ejic.201800709

[14] Doveri, L.; Taglietti, A.; Grisoli, P.; Pallavicini, P.; Dacarro, G. Dual mode antibacterial surfaces based on Prussian blue and silver nanoparticles. Dalton Trans. 2023, 52, 452–460. DOI: 10.1039/d2dt03058f

[15] Commission Regulation (EU) No 10/2011 of 14 January 2011 on plastic materials and articles intended to come into contact with food. http://data.europa.eu/eli/reg/2011/10/2025-03-16

[16] Morris, G.; Sorzabal-Bellido, I.; Bilton, M.; Dawson, K.; McBride, F.; Raval, R.; Jäckel, F.; Diaz Fernandez, Y. A. A novel self-assembly strategy for the fabrication of nano-hybrid satellite materials with plasmonically enhanced catalytic activity. Nanomaterials 2021, 11, 1580. DOI: 10.3390/nano11061580

[17] Bastús, N. G.; Merkoçi, F.; Piella, J.; Puntes, V. Synthesis of highly monodisperse citrate-stabilized silver nanoparticles of up to 200 nm: kinetic control and catalytic properties. Chem. Mater. 2014, 26, 2836–2846. DOI: 10.1021/cm500316k

[18] Schneider, C. A.; Rasband, W. S.; Eliceiri, K. W. NIH Image to ImageJ: 25 years of image analysis. Nat. Methods 2012, 9, 671–675. DOI: 10.1038/nmeth.2089

[19] Staniforth, L. Evaluation of Antimicrobial Efficacy. In Russell, Hugo & Ayliffe's: Principles and Practice of Disinfection, Preservation and Sterilization, 5th ed.; Al-Adham, I., Haddadin, R., Collier, P., Eds.; Wiley-Blackwell: Hoboken, NJ, USA, 2013; pp 236–246.

[20] Fraise, A. P.; Lambert, P. A.; Maillard, J.-Y. (Eds.) Russell, Hugo & Ayliffe's Principles and Practice of Disinfection, Preservation & Sterilization, 6th ed.; Blackwell Publishing, 2004.

[21] Pallavicini, P.; Preti, L.; Protopapa, M. L.; Carbone, D.; Capodieci, L.; Diaz Fernandez, Y. A.; Milanese, C.; Taglietti, A.; Doveri, L. Nanoparticle-imprinted silica gel for the size-selective capture of silver ultrafine nanoparticles from water. Molecules 2023, 28, 4026. DOI: 10.3390/molecules28104026

[22] Seneviratne, J.; Cox, J. A. Sol-gel materials for the solid phase extraction of metals from aqueous solution. Talanta 2000, 52, 801–806. DOI: 10.1016/S0039-9140(00)00422-7

[23] Adachi, T.; Sakka, S. The role of N,N-dimethylformamide, a DCCA, in the formation of silica-gel monoliths by sol-gel method. J. Non-Cryst. Solids 1988, 99, 118–128. DOI: 10.1016/0022-3093(88)90464-4

[24] Pallavicini, P.; Taglietti, A.; Dacarro, G.; Diaz-Fernandez, Y. A.; Galli, M.; Grisoli, P.; Patrini, M.; Santucci De Magistris, G.; Zanoni, R. Self-assembled monolayers of silver nanoparticles firmly grafted on glass surfaces: low Ag^+ release for an efficient antibacterial activity. J. Colloid Interface Sci. 2010, 350, 110–116. DOI: 10.1016/j.jcis.2010.06.019

[25] Pallavicini, P.; Bassi, B.; Chirico, G.; Collini, M.; Dacarro, G.; Fratini, E.; Grisoli, P.; Patrini, M.; Sironi, L.; Taglietti, A. et al. Modular approach for bimodal antibacterial surfaces combining photo-switchable activity and sustained biocidal release. Sci. Rep. 2017, 7, 5259. DOI: 10.1038/s41598-017-05693-3

[26] Bratsch, S. G. Standard electrode potentials and temperature coefficients in water at 298.15 K. J. Phys. Chem. Ref. Data 1989, 18, 1–21. DOI: 10.1063/1.555839

[27] Pallavicini, P.; Preti, L.; De Vita, L.; Dacarro, G.; Diaz-Fernandez, Y. A.; Merli, D.; Rossi, S.; Taglietti, A.; Vigani, B. Fast dissolution of silver nanoparticles at physiological pH. J. Colloid Interface Sci. 2020, 563, 177–188. DOI: 10.1016/j.jcis.2019.12.081

[28] Fritz, J. J. Thermodynamic properties of chloro-complexes of silver chloride in aqueous solution. J. Solution Chem. 1985, 14, 865–879. DOI: 10.1007/BF00646296

[29] Pal, S.; Tak, Y. K.; Song, J. M. Does the antibacterial activity of silver nanoparticles depend on the shape of the nanoparticle? A study of the Gram-negative bacterium Escherichia coli. Appl. Environ. Microbiol. 2007, 73, 1712. DOI: 10.1128/AEM.02218-06

[30] Chernousova, S.; Epple, M. Silver as antibacterial agent: ion, nanoparticle, and metal. Angew. Chem. Int. Ed. 2013, 52, 1636–1653. DOI: 10.1002/anie.201205923

[31] Pallavicini, P. et al. silver nanoparticles synthesized and coated with pectin: an ideal compromise for anti-bacterial and anti-biofilm action combined with wound-healing properties. J. Colloid Interface Sci. 2017, 498, 271–281.

[32] Russell, A. D.; Hugo, W. B.; Ayliffe, G. A. J. Principles and Practice of Disinfection, Preservation and Sterilization, 5th ed.; Blackwell Publishing Ltd, 2013.

[33] Sleigh, J. D.; Timbury, M. C. Notes on Medical Microbiology, 5th ed.; Churchill Livingstone, 1998.

[34] D'Agostino, A.; Taglietti, A.; Grisoli, P.; Dacarro, G.; Cucca, L.; Patrini, M.; Pallavicini, P. Seed mediated growth of silver nanoplates on glass: exploiting the bimodal antibacterial effect by near IR photo-thermal action and Ag^+ release. RSC Adv. 2016, 6, 70414–70423. DOI: 10.1039/c6ra11608f

[35] D'Agostino, A.; Taglietti, A.; Desando, R.; Bini, M.; Patrini, M.; Dacarro, G.; Cucca, L.; Pallavicini, P.; Grisoli, P. Bulk surfaces coated with triangular silver nanoplates: antibacterial action based on silver release and photo-thermal effect. Nanomaterials 2017, 7, 7. DOI: 10.3390/nano7010007

[36] World Health Organization. Evaluating Household Water Treatment Options: Health-Based Targets and Microbiological Performance Specifications; WHO Press: Geneva, 2011; p. 6. ISBN 978-92-4-154836-7.

[37] EFSA Panel on Food Additives and Nutrient Sources added to Food (ANS). Safety of silver as a food additive. EFSA Journal 2018, 16, e05235.

[39] Brinker, C. J.; Scherer, G. W. Sol–Gel Science: The Physics and Chemistry of Sol–Gel Processing; Academic Press: San Diego, 1990.

[40] Derjaguin, B.; Landau, L. Theory of the stability of strongly charged lyophobic sols and of the adhesion of strongly charged particles in solutions of electrolytes. Acta Physicochim. URSS 1941, 14, 633–662.